Investigating unconventional superconductivity in the 2D Hubbard-Kanamori model using Functional Renormalization Group (FRG)

210003218

February-May 2025

Contents

1 Abstract **3**

2 Introduction **3**

3 Theoretical Background **4**
3.1 Unconventional superconductivity 4
3.1.1 Spin-fluctuation mediated superconductivity 4
3.2 Hubbard-Kanamori Model 5
3.2.1 Tight Binding Models 5
3.2.2 Hubbard Model 6
3.2.3 Hubbard-Kanamori Model 6
3.3 Theoretical Background in FRG 6
3.3.1 Flow equation 7
3.3.2 Truncation scheme (TU^{2}FRG) 9
3.3.3 Decoupling of flow equation 10
3.3.4 Instability calculation 10

4 Computational Methods **11**
4.1 Tight-Binding Models 11
4.2 divERGe 12
4.3 Convergence of Calculation 12
4.3.1 Form factor convergence 12
4.3.2 Number of k points convergence 13

5 Results and discussion **13**
5.1 1NN Model 13
5.1.1 Superconductivity in the 1NN Model 16
5.1.2 Magnetic stripes in the 1NN Model 17

5.2 Effect of next-nearest neighbour hopping (1NNN model) 17
5.2.1 Superconductivity in the 1NNN Model 19
5.2.2 Magnetic stripes in the 1NNN model 19
5.2.3 Continous variation of next-nearest neighbour hopping 23
5.3 Effect of bi-orbital system (1NN2 model) 23

6 Conclusion and Outlook **26**

1 Abstract

Due to its structural resemblance to the high-temperature cuprate superconductors [1], the two-dimensional Hubbard model has attracted sustained scientific interest for decades. This thesis conducts a detailed analysis of the 2D Hubbard model using the truncated-unity functional Renormalisation Group (TU^{2}FRG) method, within the framework of spin-fluctuation-mediated superconductivity. The interplay between magnetism and superconductivity is explored by systematically varying model parameters such as the on-site Coulomb repulsion, chemical potential, Hund's coupling, next-nearest-neighbor hopping, and the number of orbitals per site. This approach enables the identification of clear trends in the superconducting critical (T_c) temperature and order parameter, while also providing insights into the magnetic ordering.

2 Introduction

Since its discovery in 1911 [2], superconductivity has remained a topic of great scientific interest. This phenomena, characterised by an abrupt drop in resistance at a so-called "Critical Temperature (T_c)" [3] is driven by an attractive interaction between electrons. This attractive interaction gives rise to the formation of electron pairs, famously known as "Cooper pairs" [4]. For many years after the discovery of superconductivity, physicists were convinced that BCS-Eliashberg-electron-phonon theory [4] provided a complete explanation of the electron pairing mechanism in all superconducting materials. However, in 1986, the discovery of the first heavy-fermion superconductor [5] resulted in the emergence of a whole new class of materials: Unconventional Superconductors. These are condensates of cooper pairs formed by a **different** pairing mechanism than the electron-phonon coupling predicted by BCS theory [6]. For many materials, there is no consensus on what the mechanism otherwise is.

High-Temperature superconductors are defined by having a critical temperature greater than the boiling point of Nitrogen (77K). Ever since the discovery of the first high-T_c superconductor [5], the search for "(close to-) room temperature" superconductors has been extended to all kinds of unconventional supercondutors. However, a comprehensive understanding of what drives the superconductivity is required in order to achieve this. There have been multiple attempts to model the pairing mechanism of some families of high-T_c superconductors, but they have been greatly limited by the numerical challenges that working with multi-band systems and spin-orbit coupling (SOC) present. This motivates the use of a promising technique: TU^{2}FRG [7, 8].

Motivated by these challenges and by the need for simplified yet insightful models, this work turns to the two-dimensional Hubbard model—one of the most fundamental and extensively studied frameworks in condensed matter physics. Functional Renormalisation Group (FRG) is employed to investigate the influence of the Coulomb repulsion (U) and chemical potential (μ) on the interplay between magnetism and superconductivity. This is done under the key assumption that superconductivity arises from spin-fluctuation mediation. In this work, regions of stable magnetic and superconducting order are identified, and trends in their respective ordering and critical temperatures are presented. The study is further extended by examining how variations in the next-nearest-neighbor hopping amplitude and the inclusion of a second orbital per site impact all of the above.

3 Theoretical Background

3.1 Unconventional superconductivity

As previously outlined, unconventional superconductors are those in which the Cooper pair formation is not driven by the convetional electron-phonon coupling. This section aims to outline the theoretical background behind a particular class of unconventional superconductors: Spin-fluctuation mediated superconductors.

Most generally, the Hamiltonian for a superconducting state can be described as follows:

$$\hat{H} = \hat{H}^0 + \hat{H}^{cp} \tag{1}$$

where $\hat{H}^{cp}$ describes the pairing interation that leads to the formation of a Cooper pair and is given by:

$$\hat{H}^{cp} = \sum_{k,k'} \Gamma(k,k') c^\dagger_{k,\uparrow} c^\dagger_{k',\downarrow} c_{k',\uparrow} c_{-k,\downarrow} \tag{2}$$

For many unconventional superconductors, the form of the effective pairing interaction $\Gamma(k,k')$ has remained as an unanswered question for decades.

3.1.1 Spin-fluctuation mediated superconductivity

One emerging theory for some unconventional superconductors such Iron-based or heavy-fermion compounds is that the underlying pairing mechanism is driven by spin fluctuations [9]. This section discusses how to model spin-fluctuation mediated superconductivity for the fluctuation-exchange approximation (FLEX) [10].

In such cases, the effective pairing interaction $\Gamma(k,k')$ is given by [1]:

$$\Gamma(k,k') = \frac{3}{2} U^2 \chi^S(k-k') - \frac{1}{2} U^2 \chi^C(k-k') + U \tag{3}$$

This equation is taken from Ref. [11]. Here, U is the on-site Coulumb repulsion and χ^S, χ^C are the interacting spin-susceptibilities in the Charge (C) and Spin(S) channel respectively. Their form is given below.

$$\chi^S(q) = \frac{\chi^0(q)}{1 - U\chi^0(q)} \tag{4}$$

$$\chi^C(q) = \frac{\chi^0(q)}{1 + U\chi^0(q)} \tag{5}$$

These interacting spin susceptibilities are expressed in terms of the non-interacting dynamic spin susceptibility (χ^0_{ps}) which is stated below without formal proof [9].

[1] Note that this form of pairing interaction assumes that the ratio between the fluctuation frequence (w_f) and the Fermi energy is small.

$$\chi^0_{ps}(q, i\omega) = -\sum_k \int_0^\beta d\tau G^0_{ps}(k+q\tau) G^0_{sp}(k, -\tau) e^{i\omega\tau} \tag{6}$$

The calculations presented in this project are carried out in the spin-fluctuation framework. Whilst this theory has managed to succesfully capture key features in phase diagrams of unconvential superconductors, it also has its limitations. The most relevant example is that of the cuprate phase diagram: spin-fluctuation theory is able to capture the superconducting dome and the correct order parameter [12, 13] but fails to describe the characteristic pseudo-gap [14].

3.2 Hubbard-Kanamori Model

3.2.1 Tight Binding Models

The Tight Binding Model is a central element of condensed matter physics (7). In this model, electrons are bound in orbitals (called sites) around the lattice ions. Due to the overlap between the quantum mechanical wavefunctions that describe these sites, electrons are allowed to 'hop' to neighbouring sites. The probability that this hopping process will occur is given by a tunnelling amplitude, which can be calculated using a hopping integral.

This work is carried out in the tight-binding model framework, where the magnitude of the tunnelling amplitudes is at first treated as a free parameter. The starting point is a simple nearest-neighbour hoppping tight binding model. The effect of introducing a next-nearest-neighbour hopping and an extra orbital per site is then investigated *(See Fig. 1)*.

$$\hat{H}_{TB}(\underline{\mathrm{R}}) = \sum_{ij\sigma} t_{ij} (\hat{c}^\dagger_{i\sigma} \hat{c}_{j\sigma} + h.c) \tag{7}$$

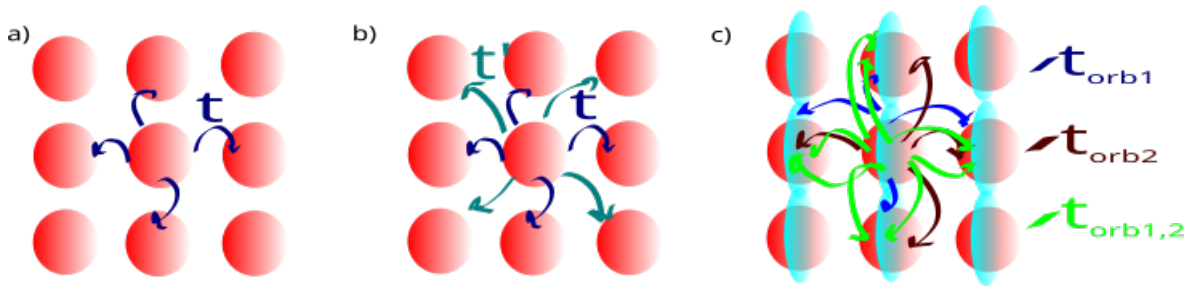

Figure 1: **Two-Dimensional Tight-Binding Models:** Three pannels showing the tight binding models for the 1NN, 1NNN and 1NN2 models discussed in Section 5.1, 5.2 and 5.3 respectively. Fig a) shows the nearest-neighbour hopping case, where t depicts the hopping amplitude between the neighbouring sites. Fig b) shows the inclusion of the next-nearest neighbour hopping, the magnitude given by t'. Fig c) Shows the extension to the two-orbital case, depicting same orbital (t_{orb1}, t_{orb2}) and different orbital ($t_{orb1,2}$) nearest-neighbour hopping. Note that this is just a pictorial representation of the orbitals, and that it does not correspond to a particular choice of orbitals or their real space projection.

3.2.2 Hubbard Model

The tight binding model as defined above fails to account for any interactions between neighbouring electrons. This motivates the extension of this model to the Hubbard model (8), which includes the (onsite) Coulomb repulsion between electrons. Despite its simple form, this model can describe very rich physical phenomena. In particular, it becomes very interesting to study when the Coulumb repulsion (U) and the nearest neighbour hoping (t) are of comparable order, since it highlights the competing phenomena that take place in correlated systems. The 2D Hubbard model remains unsolved to date, but is able to predict all sorts of correlated phases: it describes metals, insulators, superconductors and other exotic phases [15–18]. This model has been widely studied since it resembles the structure of the cuprate high-temperature superconductors [1].

$$\hat{H} = \sum_{ij\sigma} -t_{ij}(\hat{c}^{\dagger}_{i\sigma}\hat{c}_{j\sigma} + h.c) + U\sum_{i} \hat{n}_{i\uparrow}\hat{n}_{i\downarrow} \tag{8}$$

3.2.3 Hubbard-Kanamori Model

In the case of materials with a multi-band and/or multi-orbital nature, the Hubbard model is not sufficient to capture all of the physical phenomena. This motivates the extension of the Hubbard model to the Hubbard-Kanamori model [19] by including a Hund's coupling term.

$$H_{int} = U\sum_{is} n_{i,s\uparrow}n_{i,s\downarrow} + \frac{V}{2}\sum_{i,s,t\neq s} n_{is}n_{it} - \frac{J}{2}\sum_{i,s,t\neq s} \vec{S}_{is}\cdot\vec{S}_{it} + \frac{J'}{2}\sum_{i,s,t\neq s}\sum_{\sigma} c^{\dagger}_{is\sigma}c^{\dagger}_{is\bar{\sigma}}c_{it\bar{\sigma}}c_{it\sigma} \tag{9}$$

Here, U and V represent the electronic interactions in the same and different orbitals respectively. For generality, the intraorbital exchange J and the 'pair hopping' term J' following from Hund's rule coupling have been separated. Note that this Hamiltonian is relevant for the later section of this project, where the model is extended to a two-orbital, two-dimensional Hubbard model.

3.3 Theoretical Background in FRG

Solving the Hubbard-Kanamori Hamiltonian is rather challenging, which is why one resorts to numerical techniques such as FRG to do so. FRG falls into the same category of many other weak-coupling techniques (such as Mean field-theory [20], pertubation theory [21], Density Functional theory [22] or Random Phase approximation [23]). In these theories, interactions between electrons are considered to be weak. This allows one to effectively model the electrons in the system as free particles and treat their interactions as a pertubation. In the non-interacting limit, the method is therefore exact. Beyond this limit, the method's precision is controlled by the ratio between the interaction strength and the bandwidth of the system.

In this section the theoretical framework for FRG calculations is outlined. The central element of FRG is a flow equation that describes the evolution of the effective action of the system with respect to a scalar/flow parameter Lambda (Λ) *(See section 3.3.1)*. The flow equation can be solved exactly for a limited number of systems, so in most scenarios an approximation has to be

made in order to reach a solution in a reasonable computational time. (More details of how this approximation is performed and the limitations it presents can be found in Section 3.3.2). For the systems explored in this project only two-particle interactions are considered and any higher order terms are neglected. This allows the separtation of the effective action of the system into three terms. Each term represents one of the following three physical channels: Superconductivity, Spin-Density and Charge-Density Waves. The calculation is then performed to determine the "winning channel", this will correspond to the respective physical phase that the model exhibits. This rather "hand-wavy" overview of FRG is represented in a flowchart below *(See Fig.2)*. For a more rigorous explanation the reader is referred to the sections below.

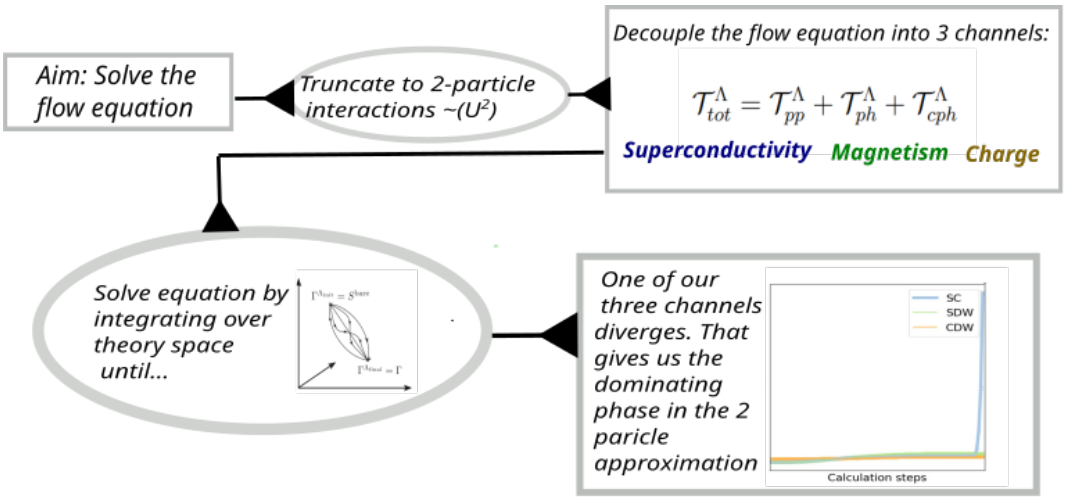

Figure 2: **FRG Flowchart:** Schematic diagram outlining the TU^{2}FRG calculation steps. Starting from the flow equation and applying the truncation scheme in order to decouple the action into three "physical" terms. The flow equation can then be solved by calculating each channel separatedly and taking the dominating phase to be the channel that diverges.

3.3.1 Flow equation

In this section the derivation of the flow equation is outlined. For such, it is assumed that the reader has grasped a strong understanding in Quantum Field theory and many-body physics. If interested in the finer details of the derivation, the reader is referred to [24].

The central elements of statitiscal physics are the partition function, the canonical potential and its Legendre transformations. These are such powerful physical quantities that one can derive all physical observables from them. For quantum many-body problems, one works instead with partition functional, defined as follows in Eq.10:

$$\mathcal{Z}[\bar{\eta}, \eta] = \int \mathcal{D}\bar{\psi}\mathcal{D}\psi e^{\mathcal{S}[\bar{\psi},\psi]} e^{(\bar{\eta},\psi)+(\eta,\bar{\psi})} \tag{10}$$

In the case of fermionic systems, the action in the exponent of Eq.10 takes the form shown below.

$$\mathcal{S}[\psi,\bar{\psi}] = -(\bar{\psi}, G_0^{-1}\psi) + V[\psi,\bar{\psi}] \tag{11}$$

Here, $V[\psi,\bar{\psi}]$ is an arbitrary many-body interaction and G_0 represents the propagator of the non-interacting system. This equation contains the shorthand notation (...), which represents the sum $\sum_x \bar{\psi}(x)(G_0^{-1}\psi)(x), (G_0^{-1}\psi)(x) = \sum_{x'} G_0^{-1}(x,x')\psi(x')$. In this sum, the Grassman field index x encodes all the quantum numbers of the single-particle basis and imaginary time.

Note that in the limiting case where $V = 0$, the path integral in Eq.10 is exactly solveable. However, the situation becomes considerably more intricate when electronic correlations are taken into account. The main idea behind FRG is to introduce a cut-off in the non interacting Green's function ($G_0 \to G_0^\lambda = f(\lambda)G_0$). This cutoff is then interpolated between the solveable intital state and the full path integral solution by susbsequently including electronic interactions. For a spin-independant system this would transform the bare propagator as shown in Equations (12) and (13).

$$G_0(k_0,\mathbf{k}) \to G_0^\lambda(k_0,\mathbf{k}) \tag{12}$$

$$\frac{1}{ik_0 - \xi_\mathbf{k}} \to \frac{\theta^\mathbf{k}}{ik_0 - \xi_\mathbf{k}} \tag{13}$$

where $\theta^\lambda(\mathbf{k})$ is defined, for example, as follows:

$$\theta^\lambda(\mathbf{k}) = \Theta(|\xi_\mathbf{k}| - \lambda) \tag{14}$$

With this particular choice of cutoff scheme, the calculation then excludes points close to the Fermi Surface *(See Fig.3)*.

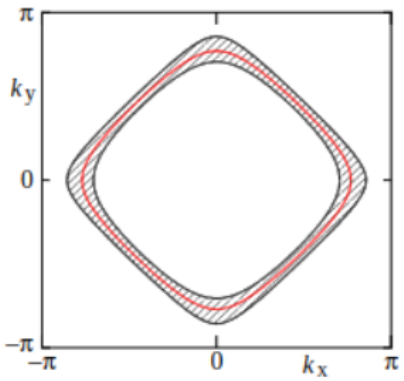

Figure 3: **Cut-off scheme example:** Momentum space region (shaded in grey) around the Fermi-surface (red) that is excluded by a momentum cut-off for a 2D square lattice with a lattice constant of 1Å. Taken from [24].

.

In the following steps the derivation will proceed in the framework of the so-called "effective action" ($\mathcal{T}[\psi,\bar{\psi}]$). This is the Legendre transformation of the Greens function functional ($\mathcal{G}[\eta,\bar{\eta}]$),

defined below in Equations (17) and (15, 16) respectively. *(For reasons that are beyond the scope of this project it is more convinient to work with the effective action than it is to do so with the partition functional.)* [2].

$$\mathcal{G}[\eta,\bar{\eta}] = -ln(\mathcal{Z}[\eta,\bar{\eta}]) \tag{15}$$

$$\mathcal{G}[\eta,\bar{\eta}] = -ln\int \mathcal{D}\psi\mathcal{D}\bar{\psi}e^{-\mathcal{S}[\psi,\bar{\psi}]}e^{(\bar{\eta},\psi)+(\bar{\psi},\eta)} \tag{16}$$

$$\mathcal{T}[\psi,\bar{\psi}] = (\bar{\eta},\psi) + (\bar{\psi},\eta) + \mathcal{G}[\eta,\bar{\eta}] \tag{17}$$

The next step is to introduce a scalar flow parameter (λ) into the generating functionals defined above. This is done in the same manner as outlined in the example shown in Equations 12 & 13. But, more generally, has to be performed such that the generators recover their orginal structure at $\lambda = 0$. After a series of algebraic manipulations, which are ommitted here but can be found in [24], one arrives at the exact functional flow equation for the effective action:

$$\frac{d}{d\Lambda}\mathcal{T}^{\Lambda}[\psi,\bar{\psi}] = (\bar{\psi},\dot{Q}_0^{\Lambda}\psi) - \frac{1}{2}\mathrm{tr}\big(\dot{Q}_0^{\Lambda}(\mathbf{\Gamma}^{(2)\Lambda}[\psi,\bar{\psi}])^{-1}\big). \tag{18}$$

Where $\Gamma^{(2)\lambda}[\psi,\bar{\psi}]$ and $\mathbf{Q}_0^{\Lambda}$ are given by equations (19) and (20) respectively.

$$\Gamma^{(2)\lambda}[\psi,\bar{\psi}] = \begin{bmatrix} \bar{\delta}\delta\Gamma[\psi,\bar{\psi}](x',x) & \bar{\delta}\bar{\delta}\Gamma[\psi,\bar{\psi}](x',x) \\ \delta\delta\Gamma[\psi,\bar{\psi}](x',x) & \delta\bar{\delta}\Gamma[\psi,\bar{\psi}](x',x) \end{bmatrix} \tag{19}$$

$$\underline{\mathrm{Q}}_0^{\Lambda} = \begin{bmatrix} Q_0^{\Lambda} & 0 \\ 0 & -Q_0^{\Lambda t} \end{bmatrix} = diag(Q_0^{\Lambda}, -Q_0^{\Lambda t}), \tag{20}$$

This flow equation is the central element of FRG and the sections below outline how to solve it.

3.3.2 Truncation scheme (TU^{2}FRG)

The flow equation derived above can be solved exactly only for a small class of systems; for most models, Functional Renormalisation Group (FRG) calculations are highly computationally expensive. In order to tackle this issue, the truncated unity approximation (TU^{2}FRG) was introduced in 2020 [7]. The main idea behind this scheme is to find a new basis that, with a controlled loss of accuracy, can represent all of the required elements in a compressed way. It can be shown that such a basis can be constructed and is well defined in the case where the calculation is constrained to terms in the order of U^2 *(two-particle interactions)* [25]. Partitions of unity [3] are then introduced into a specific part of the flow equation. This reduces an otherwise computationally expensive nested integral to a matrix product. Details of how this truncation is incorporated are ommitted but the reader is referred to Appendix. (REFERENCE appendix).

[2] If interested in why see Ref. [24]

[3] These can be essentially regarded as delta functions in momentum and real space. Their exact form can be found in [25].

Whilst the truncated scheme presents advantages in computational efficiency, particularly for models with broken translational symmetry, it also has its limitations. TU^{2}FRG relies on short-range interactions, thus struggling to capture strongly correlated phases. This is particularly relevant for the study of the 2D Hubbard model. TU^{2}FRG will not be able to capture the characteristic Mott insulating phase of the Cuprate phase diagrams [26], which limits how well the results presented in this project can be directly compared with existing literature. More importantly, the truncation scheme has a direct consquence on the accuracy of the predicted phase transition temperature (T_c). Whilst it is able to correctly capture the trends in T_c, the values predicted are much higher than what is reasonable to expect in real materials. Nevertheless, TU^{2}FRG successfully captures the competition between Magnetic and Superconducting instabilities, a central focus of the results presented in this project.

3.3.3 Decoupling of flow equation

After constraining ourselves to the case of two-particle interactions in the framework of translationally invariant systems, one can decouple the two-particle coupling as a function of the flow parameter (λ) into three channels:

$$V(k1,k2,k3) = V^{(0)}_{k_1,k_2,k_3} - \phi^{P}_{k_1+k_2,\frac{k_1-k_2}{2},\frac{k_4-k_3}{2}} + \phi^{C}_{k_1-k_3,\frac{k_1+k_3}{2},\frac{k_2+k_4}{2}} + \phi^{D}_{k_3-k_2,\frac{k_1+k_4}{2},\frac{k_2+k_3}{2}} \tag{21}$$

Here, the three channels correspond to a particle-particle, crossed particle-hole and (three) direct particle-hole terms. These are strongly related to their respective effective actions (22-24). They represent all possible ways in which two particle can interact in the correlated system. The particle-particle (P), cross-particle-hole (C) and direct-particle-hole (D) channels correspond to the Superconducting, Charge and Magnetic phases respectively.

$$\dot{\phi}^{P}_{k_1+k_2,\frac{k_1-k_2}{2},\frac{k_4-k_3}{2}} = -\mathcal{T}_{pp}(k1,k2,k3) \tag{22}$$

$$\dot{\phi}^{C}_{k_1-k_3,\frac{k_1+k_3}{2},\frac{k_2+k_4}{2}} = -\mathcal{T}_{cr-ph}(k1,k2,k3) \tag{23}$$

$$\dot{\phi}^{D}_{k_3-k_2,\frac{k_1+k_4}{2},\frac{k_2+k_3}{2}} = -\mathcal{T}_{d-ph}(k1,k2,k3) \tag{24}$$

The decoupling outlined above enables the treatment of the effective action as a separable object:

$$\mathcal{T}[\psi,\bar{\psi}] = \mathcal{T}_{pp}[\psi,\bar{\psi}] + \mathcal{T}_{ph}[\psi,\bar{\psi}] + \mathcal{T}_{cph}[\psi,\bar{\psi}] \tag{25}$$

3.3.4 Instability calculation

This section provides an outline of the procedure that follows after decoupling the effective action and flow equation (for more details the reader is refferred to [27]). A FRG calculation on the decoupled action yields the self-energy and the two-particle vertex[4]. Although these quantities

[4]For precise definitions of these quantities, see [24]

are not directly measurable, they serve as the foundation for further analysis. The first post-processing step involves identifying which of the three interaction channels diverges, revealing the leading susceptibility. Mean-field analysis is then performed at the critical scale to determine the ordering symmetry and derive a linearized gap equation. This, in turn, enables the computation of the superconducting gap and order parameter.

4 Computational Methods

This section outlines how the concepts presented above link together and are implemented for the purpose of this project. The general aim is to solve the 2D Hubbard-(Kanamori) model. This is achieved computationally, using the divERGe package *(See section 4.2)* which implements the TU^{2}FRG formalism discussed in Section 3.3.2. All of the calculations are carried out under the assumption that the superconductivity is spin-fluctuation mediated *(See section 3.1.1)*. This section outlines the methods followed to calculate the required Tight-Binding models for each of the systems, the utilisation of divERGe to solve them and some of the required convergence techniques.

4.1 Tight-Binding Models

This project investigates three models: the 1NN, 1NNN and 1NN2 model (*See Fig.1*). For the first two, the hopping parameters in the tight-binding model are treated as free parameters. For the later, the hopping parameters are determined using the method described below.

Constrained to the case of a single layer, the 1NN model is extended to a multi-orbital system by including two-orbitals per site and investigating the effect of the interorbital hopping. To allow for future comparison with existing literature [28], a choice of $d_{x^2-y^2}$ and $d_{3z^2-r^2}$ orbitals is made. The respective hopping parameters are determined using the table of interatomic matrix elements calculated by J.C. Slater and G.F. Koster [29]. In this calculation, the magnitudes of the σ, π, δ bond strength are approximated to $\approx 1, 0.5, 0.05eV$ respectively in order to capture their relative values [30–32]. A table summarising the estimated parameters for the models discussed in Section 5.3 is shown below.

Model	$t^{[1,0,0]}_{3z^2-r^2}$	$t^{[0,1,0]}_{3z^2-r^2}$	$t_{x^2-y^2}$	$t^{[1,0,0]}_{x^2-y^2-3z^2-r^2}$	$t^{[0,1,0]}_{x^2-y^2-3z^2-r^2}$
	-0.781	-0.719	-0.375	-0.402	-0.310
1NN2MN	on	on	on	off	off
1NN2MY	on	on	on	on	on

Table 1: **Nearest neighbour hopping parameters for 2D two-orbital Hubbard models.** First row shows the calculated hopping parameters. These are labelled by a lower and upper index reresenting the orbital and the direction of hoping respectively. Other rows in the table show which hopping parameters were included in each of the two models from Section 5.3.

4.2 divERGe

divERGe is an open-source, high-performance, C/C++/Python library that includes a truncated unity FRG (TU^{2}FRG) computational backend [33]. At the core of the truncated-unity calculation is a model that incorporates all the essential physical parameters. This model must accurately reflect the system's kinematics, based on its real-space hopping parameters. It is equally important to define structural details such as the Bravais lattice vectors, the number of atoms per unit cell, and the number of orbitals per atom. Once the model is established, six input parameters must be specified for the calculation to proceed: the strengths of the Coulomb repulsion (U) and Hund's coupling (J), the value of the chemical potential (μ), as well as the form factor, nk and nkf values. The latter three are discussed in more detail in Section 4.3.

With the model constructed and all necessary parameters defined, the calculation can proceed. Under the approximations described in Section 3.3.2, the flow equations are integrated numerically from high energy scales ($\lambda = \infty$) down to low scales ($\lambda = 0$), by incrementally stepping from λ to $\lambda + d\lambda$. This integration continues until a phase transition is detected—signaled by the divergence of one of the interaction channels—or until a minimum value of λ is reached. In the latter case, the system is considered to remain in a Fermi-liquid state. All such computations were performed on the high-performance computing (HPC) cluster at the University of St Andrews.

4.3 Convergence of Calculation

In the truncated-unity approximation, several convergence tests must be performed to ensure that calculations are accurate. These tests include checking the form factor convergence and the number of k points.

4.3.1 Form factor convergence

The set of orthogonal basis functions (f_m) used to describe the Truncated space*(See section 3.3.2)* in momentum representation is called the **form factor basis**. In the case of the square lattice, the form factor take the form of delta functions in real space; they are arranged as circles with increasing radii around the origin. This effectively leads to a "bond-like" representation where the form-factor number represents how many of the neighbouring bonds are accounted for in the calculation of each point in the phase diagram. For mathematical rigour on the definition of the form factor, the reader is referred to [25].

The divERGe package allows the user to modify the number of form-factor shells accordingly. Choosing an appropraite values ultimately comes down to a trade between computational accuracy and expensiveness. For the results in this project, the form factor value was set at 4Å[5] after the convergence of the the calculations was tested accordingly for a range of points in the phase diagram *(an example of such tests is shown in Fig.4)*. Moreover, this value is in agreement with values used in previous literature [25].

[5]This is equivalent to a number of form factor shells of 4 since the lattice spacing of the models here is set to 1Å.

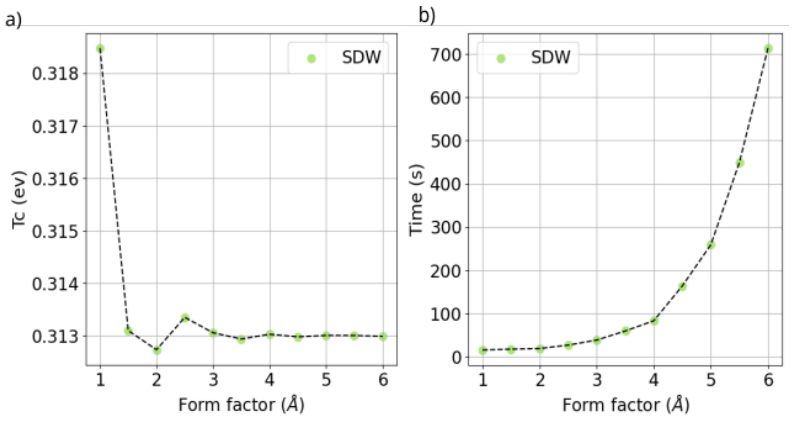

Figure 4: **Convergence testing:** Fig a) Transition temperature as a function of form factor for the 1NN model, U = 5.00, $\mu = 0.20$eV. Fig b) Time taken for calculation as a function of form factor.

4.3.2 Number of k points convergence

When integrating the flow equation, there are two parameters that can be further tuned to ensure convergence. These are the n_k and n_{k_f} values and, loosely speaking, they specify the number of k points used to carry out the nested integration of the decoupled flow equation. In particular, n_k refers to the number of k points used for the general momentum integral, and n_{k_f} to the number of k points used for the additional sum around each k-point. The calculations performed here were carried out with an integration grid of 20x5 (n_k x n_{k_f}) points. The choice of parameters ensured that the calculations had converged appropriatedly and resulted in a computational time of $\approx 180s$ per point for the simpler models.

5 Results and discussion

The results of this thesis are discussed in three sections, each focusing on one of the models outlined in Fig.1. These subsections explore the interaction between magnetism and superconductivity, highlighting trends in the superconducting order parameter and spin density wave nesting vectors. The effect of varying factors such as Coulomb repulsion, chemical potential, Hund's coupling, next-nearest-neighbor hopping, and the number of orbitals per site on the critical temperature of the superconducting regions is also examined.

5.1 1NN Model

The 1NN model is defined as the 2D Hubbard model with a single orbital per site, allowing hopping between nearest-neighbour sites *(a diagramatic representation can be found in Fig.1.a)*. As discussed in Section 3.2.2, solving this model near half-filling presents significant challenges. This section investigates the solution to the 1NN Model Hamiltonian using two-particle-interaction-truncated FRG. A phase diagram, plotted in terms of the on-site Coulomb repulsion U and chemical potential μ is presented and analyzed in detail. The calculations were performed using

a 20x5 n_kxn_{kf} grid and a form factor of 4Å, with a nearest-neighbor hopping parameter of 1eV. These convergence parameters were selected based on the methods outlined in Section 4.3. The results cover Coulomb repulsion values ranging from 1 to 20 eV and chemical potential values spanning the full energy bandwidth of the model (from -4 eV to 4 eV). While previous FRG studies on the 2D Hubbard model exist [34–36], they mostly focus on specific regions of the phase diagram. As a result, there has been limited investigation into the effects of varying the on-site Coulomb repulsion. The present work, therefore, explores a much broader range of parameters than what has been previously studied.

There are several caveats to the results presented here. In real materials, the chemical potential is an easily tuneable parameter due to its strong connection to the electronic doping of the system. In turn, controlling the magnitude of the Coulumb repulsion between electrons is far from straightforward. Additionally, some of the interesting features discussed in this report fall outside the physical regime—specifically, the FRG calculation assumes a weak-coupling limit, meaning that any Coulomb repulsion values exceeding the bandwidth of the material (8 eV) are unphysical in this context. Therefore, the analysis conducted in this project should not be interpreted as a guide to enhance superconductivity in materials that closely resemble the models studied. Instead, the primary goal is to understand how variations in certain parameters *(U, μ, t')* influence the correlated phases observed in the model. It is also important to note, as discussed in Section 3.3.2, that any analysis of the superconducting transition temperature should be treated qualitatively. At no point does this work claim to have identified superconducting regions with transition temperatures of the order of thousands of Kelvin.

The complete phase diagram for the values discussed above is shown in Fig.5. As is expected for both the Hubbard model and the Cuprates [37–39], a pronounced competition between Magnetism and Superconductivity (SC) is observed. This interplay gives rise to a prominent magnetic dome, sandwiched between two narrower d-wave superconducting regions. This magnetic dome is **Anti-Ferromagentically** (AFM) ordered and its width increases with increasing Coulumb repulsion is increased. In other words, a stronger Coulumb repulsion favours the magnetic instability as the "winner" of this magnetism/SC competition for a larger range of doping values. Both AFM and d-wave SC arise from repulsive scattering between (π,0) and (0,π) vectors. Therefore, their competition peaks closest to the Van-Hove singularity, where both instabilities are amplified and mutually reinforced [40, 41]. Aditionally, narrow magnetic stripes emerge at even-integer chemical potential values. At high values of U -those that exceed the material's bandwidth- patches of a charge density wave (CDW) instability appear around regions of the superconducting dome.

The results presented here align with previous studies of the two-dimensional Hubbard model. Dynamical Mean Field Theory (DMFT) has previously captured the coexistence of antiferromagnetic (AFM) and superconducting (SC) order parameters within the same solution across a range of doping levels (analogous to variations in μ in this work) in the weak-coupling regime. A smooth transition between these two phases has also been reported [42]. However, the FRG treatment of the 2D 1NN Hubbard model has not been able to capture certain key features of the cuprate phase diagram—namely, the Mott insulating phase and the emergence of the pseudogap that have been found in other studies of the 2D Hubbard model [43, 44].

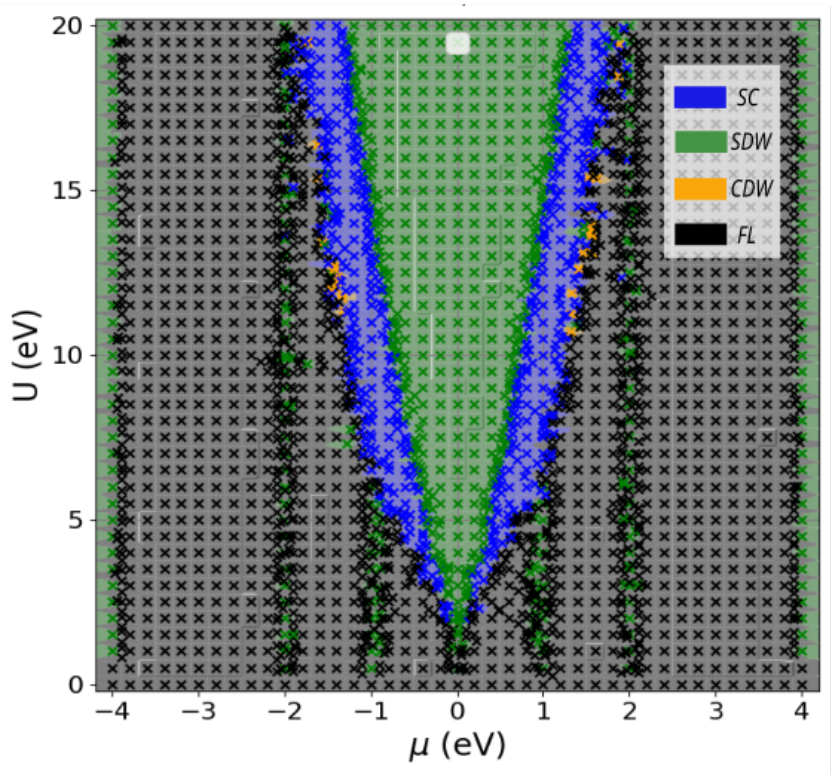

Figure 5: **Phase diagram for the 1NN model**: (t =1eV, nkxnkf = 20x5, ff = 4Å) as a function of On-site Coulumb Repulsion U and chemical potential μ. Figure shows the four phases observed in the 1NN model: SC (Superconductivity), SDW (Spin-Density Wave), CDW(Charge Density Wave) and FL (Fermi-Liquid). Calculated points in the phase diagram are showed by the 'x' markers and a lighter-couloured background is used to depict interpolated regions between these points.

5.1.1 Superconductivity in the 1NN Model

Recent findings have claimed that the 2D Hubbard model does not have a superconducting ground state [45]. Whilst the model in Ref. [45] is the same as the 1NN model explored in this section, the paper's analysis is conducted in a slightly different framework than the one used in this project: using DMRG [46] at moderate-to-strong coupling and for values of U between 6-8eV*(which the paper claims to be the regime relevant to the cuprates)*. The lack of superconductivity in their findings is attributed to a lack of competition between the magnetic and superconducting phases. Here, in the weak-coupling framework, both competition between magnetism and superconductivity and a stabilised superconducting region is found. The superconducting order parameter in this stable region is plotted on top of the Fermi-Surface for the first BZ (Fig.6a). The order parameter shows antisymmetry with respect to a 90 degree rotation and therefore one concludes that the bulk superconducting region is d-wave symmetric. This is in agreement with what is expected from the Cuprate superconductors [47].

After plotting the the critical temperature (T_c) as a function of chemical potential (μ) for a constant Coulumb repulsion(U), one observes that the superconducting critical temperature is maximised closest to the magnetic instability (Fig.6b). This is in agreement with the idea that competition between instabilities enhace the phase transition temperature [48, 49]. Moreover, the magnitude of the Coulumb repulsion and Tc are positively correlated, as is to be expected from the assumed of the pairing mechanism *(See Eq.3)*. It is important to note that limiting the interactions accounted for in the FRG calculation to two-particle interactions acts as a bottle-neck for the accuracy of the Tc values calculated. Nevertheless, the trends in Tc remain trustworthy.

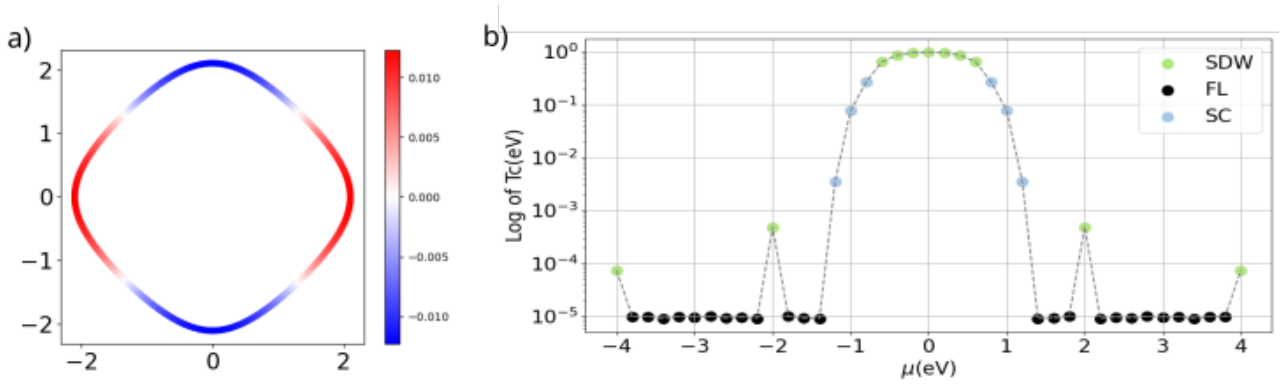

Figure 6: **Superconductivity in the 1NN model**: Fig a) Superconducting order parameter projected on Fermi Surface at $\mu = 1.00$ eV, for U =10.00eV. The order parameter is antisymmetric about a 90 degree rotation and hence it exhibits d-wave symmetry. Fig b) Transition temperature (T_c) plotted on a logarithmic scale as a function of chemical potential (μ) for U =10.00eV, showing a smooth transition between SC and SDW regions. Tc is enhanced closest to the magnetic instability. Although both plots are shown only specific for certain values of U and μ, the results they display hold for the enterity of the superconducting region of the phase diagram in Fig.5.

5.1.2 Magnetic stripes in the 1NN Model

Another distinctive feature of the Cuprates *(as well as of other unconventional superconductors* [50]*)* is the emergence of "stripes" in their phase diagram. These are patterns of alternating charge-density and spin density waves [51, 52]. In the 1NN model discussed here, these patterns are not observed. However, magnetic regions of interest are found outside the main antiferromagnetic (AFM) dome. The 1NN phase diagram in Fig.5 reveals what will henceforth be referred to as "magnetic stripes" occurring at even integer values of the chemical potential (μ). Most of them are ferromagnetically ordered and evolve to some commensurate nesting vector as the Coulumb repulsion is increased.

The physics becomes particularly interesting at a chemical potential of $\mu = 1.00eV$. In Cuprates, a doping of $\frac{1}{8}$th is known as "the magical doping" [53], where stripes emerge and superconductivity is supressed. In this model, the magical doping corresponds to a chemical potential of $\pm 1.00eV$(which is $\frac{1}{8}$th of the bandwidth). At low Coulumb repulsion values, a ferromagentically ordered spin density wave (SDW) is observed. This SDW is supressed by a superconducting phase, only to be revived at around $U \approx 15.00eV$, where it becomes antiferromagnetically ordered. The superconducting transition temperature T_c increases along the stripe *(See Fig.7)*. While this behaviour is not the same as the convetional stripes seen in cuprates, it is fair to conclude that there is still something "magical" about the $\frac{1}{8}$ filling fraction in the 1NN model presented here.

It is worth noting that before conducting this analysis, the possibility of the stripes being a computational artifact was ruled out. This was done by increasing the n_kxn_{k_f} resolution for a single point in the stripe and confirming that the result remained unchanged. The appearance of these stripes as true outcomes of the calculations is further validated in Section 5.2.2.

5.2 Effect of next-nearest neighbour hopping (1NNN model)

The 1NNN model is an extension of the 1NN model described in previous sections, incorporating the next-nearest neighbour hopping amplitude as an additional free parameter. This section presents three additional phase diagrams for the two-dimensional Hubbard model, with next-nearest neighbour hopping amplitudes of 0.25, 0.50 and 0.75 eV *(See Fig.8)*. The nearest neighbour hopping amplitude remains fixed at 1eV for all models. Furthermore, the chemical potential of the models is adjusted to ensure a constant number of electrons at half-filling, to allow for a direct comparison between the models.

As the next-nearest neighbour hopping is increased, the position of the Van-Hove singularity shifts to lower energies *(See Fig.8a)*. This increase in t' also alters the Fermi-surface, which in turn changes the nesting vectors of the models. As a result of both these effects, the SC-SDW-SC sandwich region shifts toward the negative chemical potential regime as t' increases. The superconducting regions remain (in the most-part) d-wave symmetric and the emergence of magnetic stripes remains observable. Additionally, general trends in the superconducting transition temperature (T_c) are also observed: it is maximised closest to the magnetic instability and it increases as a function of U.

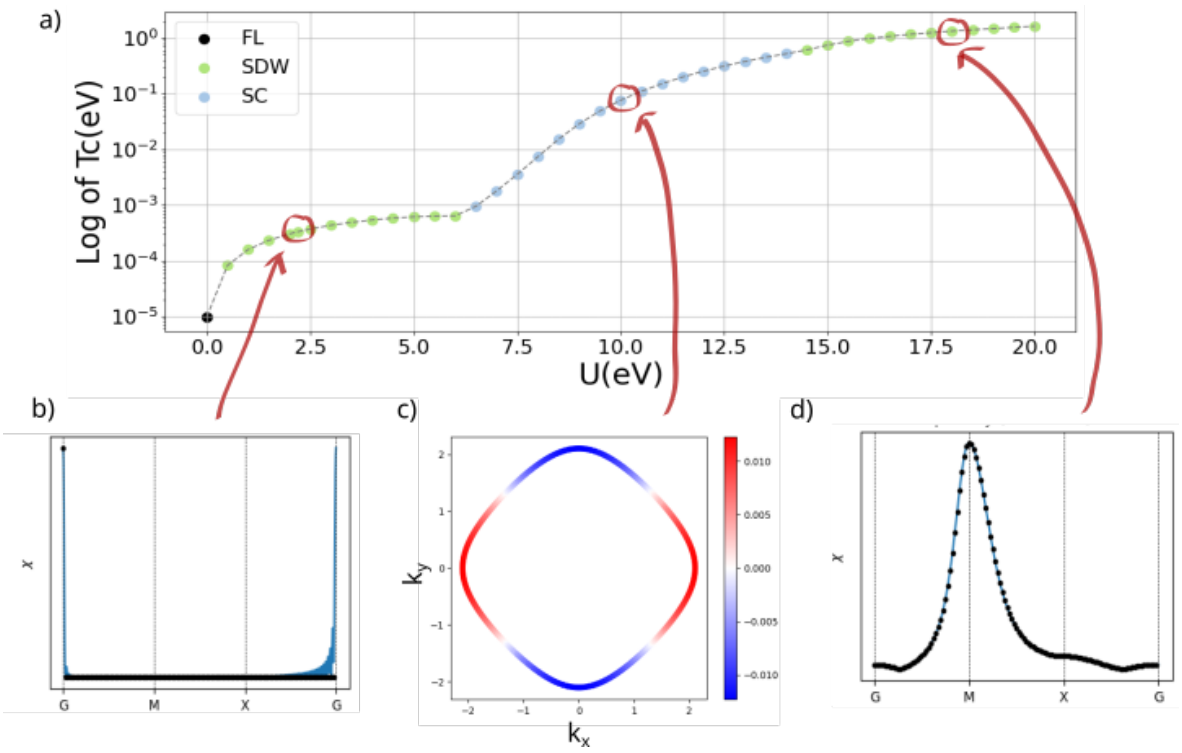

Figure 7: **Magnetic stripe in the 1NN model for doping at $\frac{1}{8}$ of the bandwith**: Fig a) Transition temperature plotted in a Logarithmic scale as a function of Coulumb repulsion (U) along the Magnetic stripe at μ =1eV. Fig b) Magnetic susceptibility along high symmetry path for U =2.00 eV. Fig c) Plot of the Superconducting order parameter projected on top of the Fermi-surface of the 1NN model for U = 10.00eV and μ =1.00eV. Fig d) Magnetic susceptibility along high symmetry path for U= 18.00eV. The plots show the susceptibility as a function of $\underline{q}$ for both magnetic regions. The Ferromagnetic SDW is supressed by a superconducting phase at U$\approx$ 6.00eV. At larger values of U, the SDW phase is recovered but with an Anti-Ferromagnetic ordering instead.

Several studies have explored the effect of t' in the 2D Hubbard model, employing both FRG [54] and other alternative methods [55], with a particular focus on using t' as a means to enhance T_c. The results presented here take a slightly different approach, aiming to compare the features of the 1NN and 1NNN phase diagrams.

5.2.1 Superconductivity in the 1NNN Model

Including a next-nearest neighbour hopping parameter in the 1NN model does not lead to many significant changes in the superconducting properties of the model. The order parameter is predominantly d-wave symmetric and the superconducting temperature (T_c) increases with Coulumb repulsion. Proximity to a Magnetic instability further enhances T_c. Additionally, the same SC-SDW-SC sandwich structure is observed even after breaking particle-hole symmetry, reinfocing the idea that that superconductivity is favoured in the vicinity of a spin density wave (SDW) instability.

While most key features remain unchanged, there is an important difference between the superconducting regions in the 1NN and 1NNN model. When $t' \neq 0$, charge density wave (CDW) patches appear neighbouring some superconducting regions. Specifically, when $\frac{t'}{t} = 0.75$, and for Coulumb repulsion between 8 and 11eV, the superconducting order parameter undergoes a change. Along these horizontal cuts there is a SCI-SDW-SCII-CDW transition. The Superconducting order parameter is always d-wave symmetric in the SCI region and for most of the SCII region, but it abruptly transitions to s-wave symmetric in the vicinity of the CDW region *(See Fig.9)*. This behaviour is also observed in the SC regions that neighbour CDW regions for the $t' = 0.25, 0.50eV$ models. To confirm whether this represents a physical phase transition, one would expect to experimentally observe a discontinuity as a result of an additional symmetry breaking when the order parameter shifts from s-wave to d-wave symmetry.

5.2.2 Magnetic stripes in the 1NNN model

The presence of magnetic stripes is another common feature shared by the 1NN and 1NNN models, further supporting its physical origin. A summary of all the stripes and their respective nesting vectors is provided in Table.2. The locations of these stripes suggest that their formation is a consequence of strong nesting at specific chemical potential values. Notably, the stripe at "magic doping" is the only to undergo a change ordering from ferromagnetic (FM) to antiferromagnetic (AFM) as a result of the strong competition with Superconductivity.

While the transition from a Fermi liquid phase to any of the superconducting (SC), spin density wave (SDW), or charge density wave (CDW) phases is quite abrupt, the critical temperature evolves more smoothly for stripes where there is a strong competition between SC and SDW/CDW instabilities *(see Fig.10)*. This is consistent with the discussion in Section 5.1.2. When $\frac{t'}{t} = 0.50$, a magnetic double dome emerges, becoming more pronounced as the Coulomb repulsion increases *(see Fig.11)*. This is the pattern one might expect in the superconducting region, as observed in cuprates [56]. However, this trend is only observed in this particular model and phase.

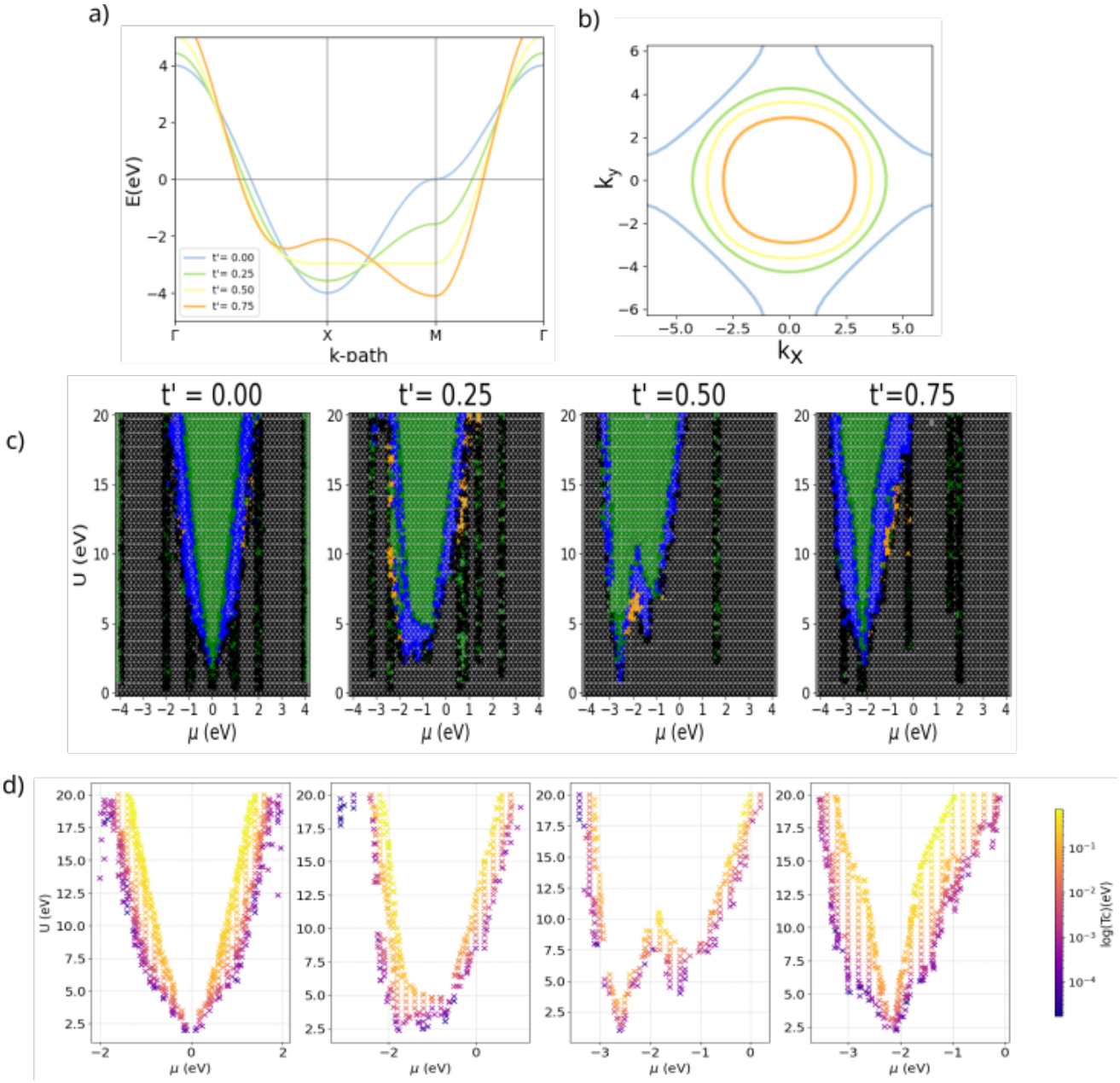

Figure 8: **1NNN model:** a) Single plot of the band structure along high-symmetry path for corresponding values of t'. b) Single plot of the Fermi surface for all values of t' considered. c) Phase diagram for the 1NNN model as a function of Coulumb repulsion U and chemical potential μ (t =1eV, nkxnkf = 20x5, ff = 4Å) for t'=0.00, 0.25, 0.50, 0.75 eV. d) Transition temperature for the superconducting region (plotted in a logarithmic scale).

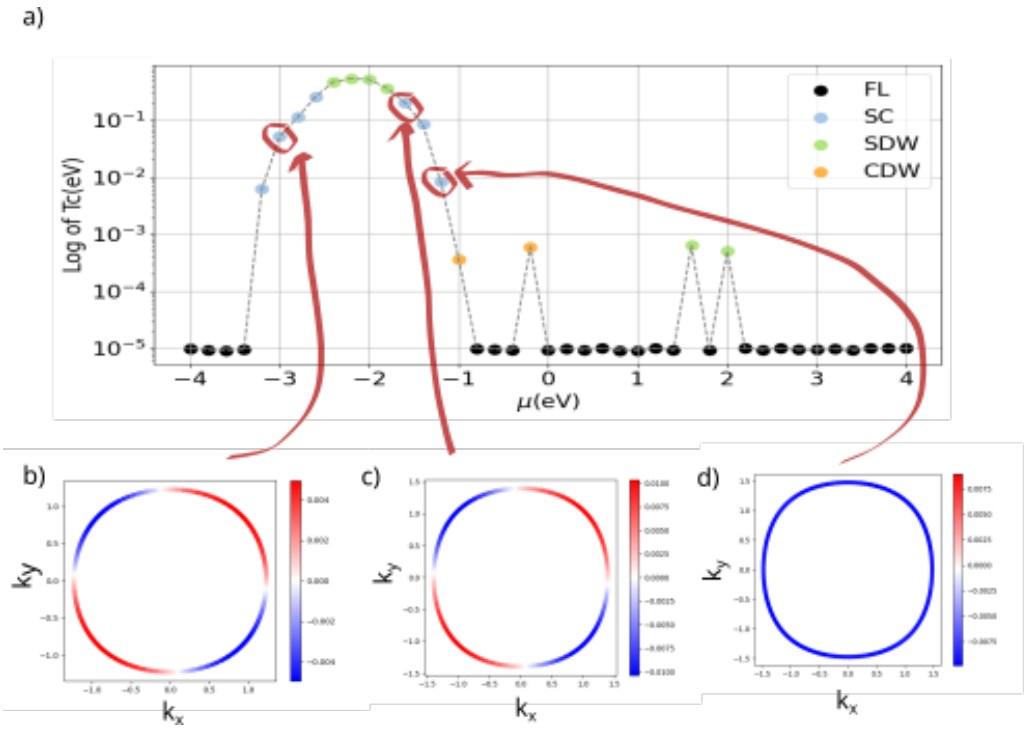

Figure 9: **Change in the superconducting order parameter in the t' =0.75eV 1NNN model**: Fig a) Critical temperature plotted in a Logarithmic scale as a function of chemical potential μ for U = 11.50eV. The lower panel shows the magnitude of the superconducting order parameter plotted on top of the fermi surface for U= 11.50eV and μ = -3.0eV, -1.6eV and -1.2eV. These are shown in Figs b) c) and d) respectively.

t'(eV)	μ (eV)	Competing with other phase?	Nesting vector	Magnetic ordering
0.00	1.00	Yes (SC)	(0,0)-(π, π)	FM-AFM
0.00	2.00	No	(0,0)-(0, π)	FM-Commensurate
0.25	-3.20	No	(0,0)	FM
0.25	-2.40	No	(0,0)	FM
0.25	-2.00	No	(0,0)-(π, π)	FM - AFM
0.25	0.60	No	(0,0)	FM
0.25	1.40	Yes (CDW)	(0,0)	FM
0.25	2.40	No	(0,0)	FM
0.50	-2.60	No	(0,0)	FM
0.50	1.60	No	(0,0)	FM
0.75	-3.00	Yes(SC)	(0,0)	FM
0.75	-2.20	Yes(SC)	(0,0)-inc.	FM- Incommensurate
0.75	2.00	No	(0,0).	FM

Table 2: **Survey of stripes in the 1NNN model.** Table summarising the location and magnetic ordering of the Stripes in the 1NNN model .

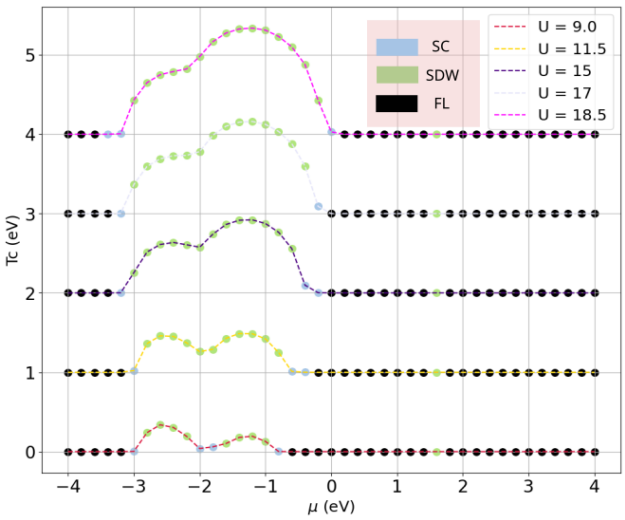

Figure 11: **Magentic Dome in 1NNN, t'=0.50eV model**: T_c as a function of μ for different values of U (offsetted by 1eV). This figure shows how the height of the second magentic dome increases as a function of U whilst the height of the first remains constant. The turning point of the double dome pattern occurs at μ=-2.00eV

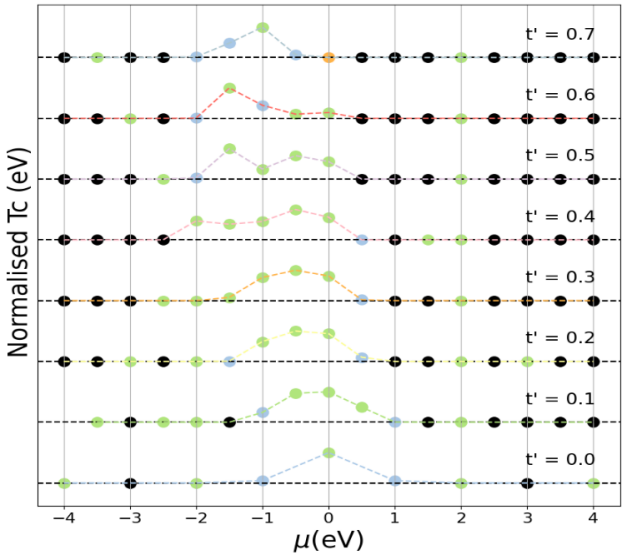

Figure 12: **Continuous variation of t':** Normalised T_c plotted as a function of chemical potential μ for several values of t'. T_c is normalised separatedly with respect to the maxima of each plot in order to allow for the clear vizualisation of the trend as μ is varied.

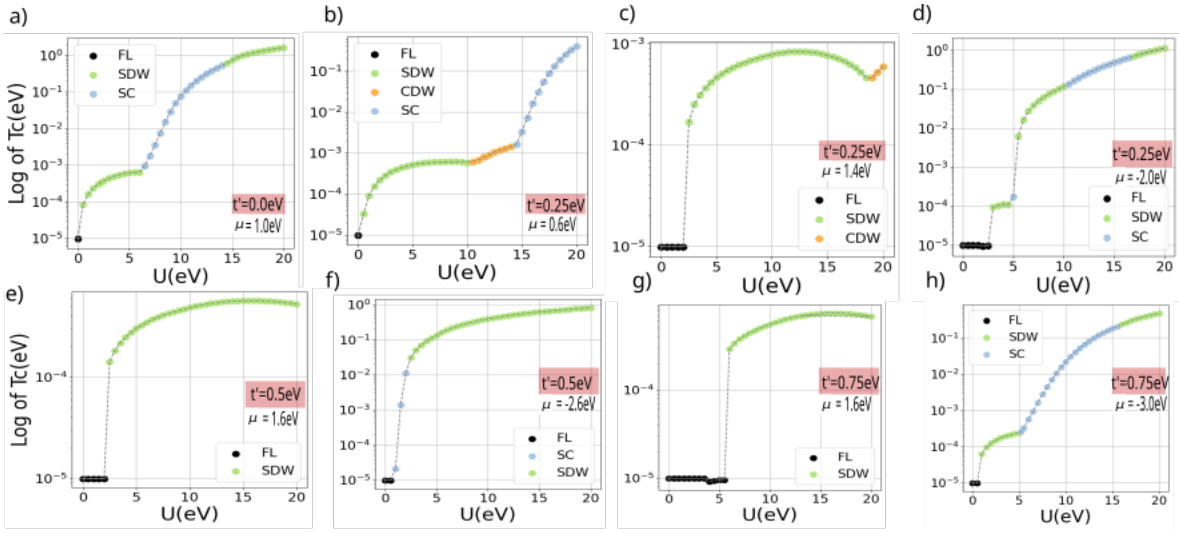

Figure 10: T_c **as a function of Coulumb repulsion for a selection of stripes in the 1NNN model**: T_c plotted in a logarithmic scale for stripes at: Fig a) t' = 0.00eV, μ=1.00eV, b) t' = 0.25eV, μ=0.60eV, c) t' = 0.25eV, μ=1.40eV, d) t' = 0.25eV, μ=-2.00eV, e) t' = 0.50eV, μ=1.60eV, f) t' = 0.50eV, μ=-2.60eV, g) t' = 0.75eV, μ=1.60eV, h) t' = 0.75eV, μ=-3.00eV. Showing abrupt jumps in the critical temperature in FL-(SC,SDW,CDW) phases and a smoother evolution for any SC-SDW/CDW transitions.

5.2.3 Continous variation of next-nearest neighbour hopping

In order to further support the ideas discussed in Section 5.1, the critical temperature is plotted as a function of chemical potential μ for different values of t' at U=10.00eV *(See Fig.12)* The magnetic region is pushed towards more negative values of the chemical potential as the value of the next-nearest neighbour hoping parameter is increased (and the van Hove singularity is pushed down in energy). The bulk magnetic region remains antiferromagnetically ordered and the SC order parameter is predominantly d-wave symmetric. The exception occurs when t' is set to 0.70eV. There, the SC order parameter transitions to s-wave symmetric when it is closest to the boundary with the charge density wave (CDW) phase *(as discussed in Section 5.2.1)*.

5.3 Effect of bi-orbital system (1NN2 model)

The models presented so far were constructed assuming a single orbital per site. This section discusses the effect of incorportaing two orbitals per site. The model was calculated using the parameters discussed in Section 4.1 and with the inclusion of multiple orbitals per site, the Hamiltonian is extended to the Hubbard-Kanamori form *(See Section 3.2.3)*. The chemical potential is fixed at both the undoped ($\mu = 0.00eV$) and doped ($\mu = 1.00eV$) levels. The Coulumb repulsion and Hunds coupling strengths are varied from 1-10eV and 0.1-1.0eV, respectively. The calculations were carried out using a form factor of 4Åand an n_kxn_{k_f} grid of 20x5. This section first discusses the 1NN2MY model, where orbital mixing between different orbitals is set to zero, and compares it later with the 1NN2MN model, which includes this orbital mixing.

In the undoped case, the model exhibits an antiferromagnetically ordered spin density wave (SDW) ground state for $U > 3.00eV$. When the coulomb repulsion is set to zero, the groundstate transitions to a charge density wave (CDW) with a (π, π) nesting vector. Doping the system to a chemical potential of $\mu = 1.00eV$ supresses the SDW, and instead, a small superconducting patch emerges in the boundary of the CDW phase *(See Fig.13)*. The magnitude of the Hund's coupling has a minor effect in the dominating phase and its transition temperature (T_c). The Superconducting regions shown in Fig.13.d exhibit different order parameters. The SC region at U=0.0eV is s-wave symmetric whilst the SC region at U =10.00eV is d-wave symmetric. By comparing Figures 13c,d with e,f, it can be concluded that the inclusion of different orbital hopping promotes the emergence of a CDW phase at lower Coulomb repulsion values in the doped case with $\mu = 1.00eV$.

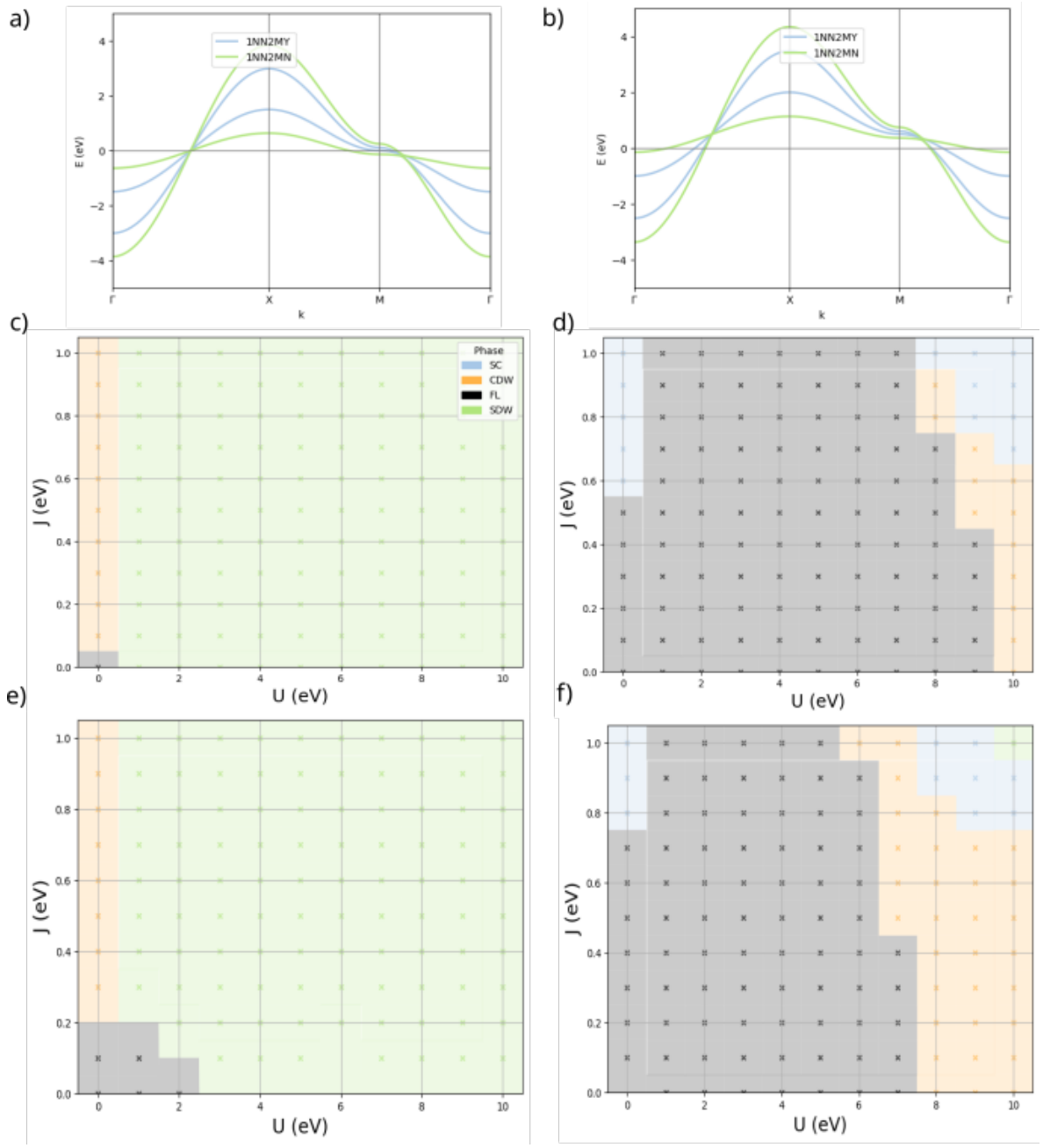

Figure 13: **Phase diagram for the 1NN2 model:** Phase diagram for the 1NN2 model without orbital mixing between different orbitals. Fig a) Band structure for the undoped 1NN2MY/N model. Fig b) Band structure for the 1NN2MY/N model at $\mu = 1.0eV$. Fig c) Phase diagram for the undoped 1NN2MY model. Fig d) Phase diagram for the 1NN2MY model at $\mu = 1.00eV$. Fig e) Phase diagram for the undoped 1NN2MN model. Fig f) Phase diagram for the 1NN2MN model at $\mu = 1.00eV$.

6 Conclusion and Outlook

This project aimed to investigate the interplay between Magnetism and Superconductivity in the 2D Hubbard Model at half-filling. The calculations were carried out in the spin-fluctuation mediated superconductivity framework using the two-particle truncated TU^{2}FRG scheme in the weak-coupling limit. Although this method fails to capture correlated phases such as Mott-instulating or pseudo-gap phases, it is widely in agreement with previous literature. The results presented here provide a comprehensive study of this model for a uniquely wide range of parameters. A strong competition between an Antiferromagnetically-ordered SDW and d-wave symmetric SC phase is observed. Additionally, several strategies to stabilize and enhance the critical temperature of superconductivity are identified, including increasing the on-site Coulomb repulsion and being near a stabilized SDW region. Narrow magnetic stripes are present, with their ordering changing at the "magical doping" value. The effect of including a next-nearest neighbor hopping parameter is examined in detail. Increasing t' lowers the Van Hove singularity's energy, shifting the region of prominent SDW-SC interplay towards more negative chemical potentials. A magnetic double dome emerges for a ratio of $\frac{t'}{t} = 0.50$. The inclusion of t' also leads to stable charge density wave (CDW) patches surrounding SC regions, where the SC order parameter transitions from d-wave to s-wave symmetry near these patches. Finally, a preliminary analysis is provided on extending these models to a two-orbital-per-site case. The AFM ground state is suppressed as the model is electronically doped, and the magnitude of Hund's coupling has minimal impact on the observed phases.

Future work could involve a more in-depth analysis of the two-orbital-per-site model, potentially exploring broader ranges of chemical potential and Hund's coupling values. Additionally, extending the study to a bi-layer, two-orbital-per-site Hubbard model would be an intriguing direction. One could also investigate the impact of spin-orbit coupling (SOC) on the results obtained. Such extensions would quickly evolve into a multi-dimensional analysis, offering numerous avenues for exploration. However, a particularly relevant direction would be to progressively increase the complexity of these models to better approximate the behavior of unconventional superconductors, such as lanthanum nickelate. This approach would involve a step-by-step examination of how the critical temperature (T_c) and superconducting regions change as model parameters evolve. Ultimately, this could provide valuable insights into the key parameters influencing superconducting phases in unconventional materials.

References

[1] Elbio Dagotto. Correlated electrons in high-temperature superconductors. *Reviews of Modern Physics*, 66(3):763, 1994.

[2] H Kamerlingh Onnes. The superconductivity of mercury. *Comm. Phys. Lab. Univ. Leiden*, 122:124, 1911.

[3] Theodore H Geballe, Robert H Hammond, and Phillip M Wu. What tc tells. *Physica C: Superconductivity and Its Applications*, 514:9–16, 2015.

[4] J Robert Schrieffer. *Theory of superconductivity*. CRC press, 2018.

[5] J George Bednorz and K Alex Müller. Possible high t c superconductivity in the ba- la- cu- o system. *Zeitschrift für Physik B Condensed Matter*, 64(2):189–193, 1986.

[6] JE Hirsch, MB Maple, and F Marsiglio. Superconducting materials classes: Introduction and overview, 2015.

[7] Christian J Eckhardt, Carsten Honerkamp, Karsten Held, and Anna Kauch. Truncated unity parquet solver. *Physical Review B*, 101(15):155104, 2020.

[8] Jonas B Profe, Luke C Rhodes, Matteo Dürrnagel, Rebecca Bisset, Carolina A Marques, Shun Chi, Tilman Schwemmer, Ronny Thomale, Dante M Kennes, Chris A Hooley, et al. Magic angle of sr 2 ruo 4: Optimizing correlation-driven superconductivity. *Physical Review Research*, 6(4):043057, 2024.

[9] Toru Moriya and Kazuo Ueda. Spin fluctuations and high temperature superconductivity. *Advances in Physics*, 49(5):555–606, 2000.

[10] Gökhan Esirgen and NE Bickers. Fluctuation-exchange theory for general lattice hamiltonians. *Physical Review B*, 55(4):2122, 1997.

[11] AB Migdal. Interaction between electrons and lattice vibrations in a normal metal. *Sov. Phys. JETP*, 7(6):996–1001, 1958.

[12] Toru Moriya. Developments of the theory of spin fluctuations and spin fluctuation-induced superconductivity. *Proceedings of the Japan Academy, Series B*, 82(1):1–16, 2006.

[13] Douglas J Scalapino. The case for dx2- y2 pairing in the cuprate superconductors. *Physics Reports*, 250(6):329–365, 1995.

[14] Tom Timusk and Bryan Statt. The pseudogap in high-temperature superconductors: an experimental survey. *Reports on Progress in Physics*, 62(1):61, 1999.

[15] Steven R White, Douglas J Scalapino, Robert L Sugar, EY Loh, James E Gubernatis, and Richard T Scalettar. Numerical study of the two-dimensional hubbard model. *Physical Review B*, 40(1):506, 1989.

[16] Jorge E Hirsch. Two-dimensional hubbard model: Numerical simulation study. *Physical Review B*, 31(7):4403, 1985.

[17] Philip W Anderson. "luttinger-liquid"behavior of the normal metallic state of the 2d hubbard model. *Physical review letters*, 64(15):1839, 1990.

[18] Kai Sun, Zhengcheng Gu, Hosho Katsura, and S Das Sarma. Nearly flatbands with nontrivial topology. *Physical review letters*, 106(23):236803, 2011.

[19] Alexei Sherman. Hubbard-kanamori model: spectral functions, negative electron compressibility, and susceptibilities. *Physica Scripta*, 95(9):095804, 2020.

[20] Leo P Kadanoff. More is the same; phase transitions and mean field theories. *Journal of Statistical Physics*, 137:777–797, 2009.

[21] Naoto Nagaosa. *Quantum field theory in condensed matter physics*. Springer Science & Business Media, 2013.

[22] Walter Kohn and Lu Jeu Sham. Self-consistent equations including exchange and correlation effects. *Physical review*, 140(4A):A1133, 1965.

[23] David Bohm and David Pines. A collective description of electron interactions. i. magnetic interactions. *Physical Review*, 82(5):625, 1951.

[24] Walter Metzner, Manfred Salmhofer, Carsten Honerkamp, Volker Meden, and Kurt Schönhammer. Functional renormalization group approach to correlated fermion systems. *Reviews of Modern Physics*, 84(1):299–352, 2012.

[25] Julian Lichtenstein. *Functional renormalization group studies on competing orders in the square lattice*. PhD thesis, Dissertation, RWTH Aachen University, 2018, 2018.

[26] Masatoshi Imada, Atsushi Fujimori, and Yoshinori Tokura. Metal-insulator transitions. *Reviews of modern physics*, 70(4):1039, 1998.

[27] Jonas Benedikt Profe. *Functional renormalization group developments for correlations in quantum materials*. PhD thesis, Dissertation, RWTH Aachen University, 2023, 2023.

[28] Hirofumi Sakakibara, Naoya Kitamine, Masayuki Ochi, and Kazuhiko Kuroki. Possible high t c superconductivity in la 3 ni 2 o 7 under high pressure through manifestation of a nearly half-filled bilayer hubbard model. *Physical Review Letters*, 132(10):106002, 2024.

[29] John C Slater and George F Koster. Simplified lcao method for the periodic potential problem. *Physical review*, 94(6):1498, 1954.

[30] Stephen J Blanksby and G Barney Ellison. Bond dissociation energies of organic molecules. *Accounts of chemical research*, 36(4):255–263, 2003.

[31] John E McGrady. Introduction and general survey of metal–metal bonds. *Molecular Metal-Metal Bonds: Compounds, Synthesis, Properties*, pages 1–22, 2015.

[32] Andreas Krapp, Matthias Lein, and Gernot Frenking. The strength of the σ-, π-and δ-bonds in re 2 cl 8 2-. *Theoretical Chemistry Accounts*, 120:313–320, 2008.

[33] Jonas Profe, Dante M Kennes, and Lennart Klebl. diverge implements various exact renormalization group examples. *SciPost Physics Codebases*, page 026, 2024.

[34] Jacob Beyer, Jonas B Profe, Lennart Klebl, Tilman Schwemmer, Dante M Kennes, Ronny Thomale, Carsten Honerkamp, and Stephan Rachel. Rashba spin-orbit coupling in the square-lattice hubbard model: A truncated-unity functional renormalization group study. *Physical Review B*, 107(12):125115, 2023.

[35] Cornelia Hille, Fabian B Kugler, Christian J Eckhardt, Yuan-Yao He, Anna Kauch, Carsten Honerkamp, Alessandro Toschi, and Sabine Andergassen. Quantitative functional renormalization group description of the two-dimensional hubbard model. *Physical Review Research*, 2(3):033372, 2020.

[36] Demetrio Vilardi, Pietro M Bonetti, and Walter Metzner. Dynamical functional renormalization group computation of order parameters and critical temperatures in the two-dimensional hubbard model. *Physical Review B*, 102(24):245128, 2020.

[37] Steven A Kivelson, Eduardo Fradkin, and Victor J Emery. Electronic liquid-crystal phases of a doped mott insulator. *Nature*, 393(6685):550–553, 1998.

[38] Eduardo Fradkin, Steven A Kivelson, and John M Tranquada. Colloquium: Theory of intertwined orders in high temperature superconductors. *Reviews of Modern Physics*, 87(2):457–482, 2015.

[39] Tuomas I Vanhala and Päivi Törmä. Dynamical mean-field theory study of stripe order and d-wave superconductivity in the two-dimensional hubbard model. *Physical Review B*, 97(7):075112, 2018.

[40] Nobuo Furukawa, TM Rice, and Manfred Salmhofer. Truncation of a two-dimensional fermi surface due to quasiparticle gap formation at the saddle points. *Physical review letters*, 81(15):3195, 1998.

[41] Carsten Honerkamp and Manfred Salmhofer. Temperature-flow renormalization group and the competition between superconductivity and ferromagnetism. *Physical Review B*, 64(18):184516, 2001.

[42] Massimo Capone and G Kotliar. Competition between d-wave superconductivity and antiferromagnetism in the two-dimensional hubbard model. *Physical Review B—Condensed Matter and Materials Physics*, 74(5):054513, 2006.

[43] AA Katanin, A Toschi, and K Held. Comparing pertinent effects of antiferromagnetic fluctuations in the two-and three-dimensional hubbard model. *Physical Review B—Condensed Matter and Materials Physics*, 80(7):075104, 2009.

[44] Junya Otsuki, Hartmut Hafermann, and Alexander I Lichtenstein. Superconductivity, antiferromagnetism, and phase separation in the two-dimensional hubbard model: A dual-fermion approach. *Physical Review B*, 90(23):235132, 2014.

[45] Mingpu Qin, Chia-Min Chung, Hao Shi, Ettore Vitali, Claudius Hubig, Ulrich Schollwöck, Steven R White, Shiwei Zhang, and (Simons Collaboration on the Many-Electron Problem). Absence of superconductivity in the pure two-dimensional hubbard model. *Physical Review X*, 10(3):031016, 2020.

[46] Steven R White. Density matrix formulation for quantum renormalization groups. *Physical review letters*, 69(19):2863, 1992.

[47] CC Tsuei and JR Kirtley. Pairing symmetry in cuprate superconductors. *Reviews of Modern Physics*, 72(4):969, 2000.

[48] M Brian Maple. Interplay between superconductivity and magnetism. *Physica B: Condensed Matter*, 215(1):110–126, 1995.

[49] JP Sun, K Matsuura, GZ Ye, Y Mizukami, M Shimozawa, Kazuyuki Matsubayashi, M Yamashita, T Watashige, Shigeru Kasahara, Y Matsuda, et al. Dome-shaped magnetic order competing with high-temperature superconductivity at high pressures in fese. *Nature communications*, 7(1):12146, 2016.

[50] Barbara Goss Levi. Are stripes a universal feature of high-t c superconductors? *Physics Today*, 51(6):19–22, 1998.

[51] Oron Zachar, SA Kivelson, and VJ Emery. Landau theory of stripe phases in cuprates and nickelates. *Physical Review B*, 57(3):1422, 1998.

[52] Matthias Vojta. Lattice symmetry breaking in cuprate superconductors: stripes, nematics, and superconductivity. *Advances in Physics*, 58(6):699–820, 2009.

[53] Seiki Komiya, Han-Dong Chen, Shou-Cheng Zhang, and Yoichi Ando. Magic doping fractions for high-temperature superconductors. *Physical review letters*, 94(20):207004, 2005.

[54] Christoph Husemann and Walter Metzner. Incommensurate nematic fluctuations in the two-dimensional hubbard model. *Physical Review B—Condensed Matter and Materials Physics*, 86(8):085113, 2012.

[55] Rodrigo A Fontenele, Natanael C Costa, Thereza Paiva, and Raimundo R dos Santos. Effects of next-nearest neighbor hopping on the pairing and critical temperatures of the attractive hubbard model on a square lattice. *arXiv preprint arXiv:2503.06753*, 2025.

[56] Louis Taillefer. Scattering and pairing in cuprate superconductors. *Annu. Rev. Condens. Matter Phys.*, 1(1):51–70, 2010.